Alkaline earth metal alloys of Cu for enhanced catalytic activity toward CO_2 hydrogenation

Kavita Thakkar[†,‡] and Kavita Joshi [*,†,‡]

†*Physical and Materials Chemistry Division, CSIR-National Chemical Laboratory, Dr. Homi Bhabha Road, Pashan, Pune-411008, India*

‡*Academy of Scientific and Innovative Research (AcSIR), Sector 19, Kamla Nehru Nagar, Ghaziabad-201002, India*

E-mail: k.joshi@ncl.res.in

Abstract

CO_2, a well-known greenhouse gas, is a potential raw material used to produce various chemicals. Dissociation of CO_2 to CO or hydrogenation to formate (HCOO) or carboxyl (COOH) intermediate is crucial in determining the reaction pathway for CO_2 conversion. In this work, we demonstrate that alloys of Mg-Cu exhibit greater activity toward activation and hydrogenation of CO_2 than transition metal alloys reported so far. Two different compositions of Mg-Cu, namely Mg_2Cu and $MgCu_2$, have been studied using periodic Density Functional Theory (DFT). Our investigations reveal that CO_2 chemisorbs on both bimetallic alloys. Coadsorption of CO_2 with H_2O leads to the spontaneous formation of $COOH^*$ over $Mg_2Cu(224)$, whereas a negligible barrier (0.04 eV) is observed for $MgCu_2$ (311). $HCOO^*$ formation has a barrier of 0.34 eV and 0.42 eV on $Mg_2Cu(224)$ and $MgCu_2(311)$, respectively. Dissociation of CO_2 to CO is kinetically unfavorable on both compositions of Mg-Cu. We provide a rationale for the observed activity by analyzing the electronic structure. Notably, the spontaneous

hydrogenation of CO_2 makes earth-abundant metals suitable candidates for alloying that await experimental verification.

Introduction

CO_2 is an unavoidable output of all the anthropogenic activities post-industrial revolution. However, it is gaining attention as a chemical feed stock in a world with carbon-based energy. It could be converted to value-added chemicals like methanol, formic acid, methane, and higher alcohols/hydrocarbons.[1–5] The foremost step of CO_2 conversion is activating/breaking the C-O bond. CO_2 activation has been widely studied on various transition metal surfaces,[6–8] metal alloys,[9–12] and metal oxides.[13–16] These investigations reveal that chemisorption is favorable over early-transition metals, whereas CO_2 physisorbs over post-transition metals Surface inhomogeneity of bimetallic alloys and metal oxides activates the CO bond more than that of flat facets of pure metals.

Two possible pathways have been proposed for the hydrogenation of CO_2. The first one is the direct hydrogenation of CO_2 to formate ($HCOO^*$) or carboxyl ($COOH^*$) intermediate. Alternatively, CO_2 can be dissociated to CO + O followed by hydrogenation of CO.[17] Bimetallic alloys have been explored as a potential candidate for selective hydrogenation of CO_2 to various chemicals.[18–24] The First step of CO_2 hydrogenation, i.e. formation of $COOH^*$/$HCOO^*$ intermediate is crucial in determining the reaction pathway. In Tab.1,

Table 1: Reported bimetallic catalysts which are investigated through DFT, favorable path, activation barrier (eV) and final product.

Catalysts	Favorable path	Activation barrier (eV)	Product
PdCu(111)	HCOO	0.62	CH_3OH[25]
$PdCu_3$(111)	HCOO	1.29	CH_3OH[25]
CuFe(100)	HCOO	0.39	C_2H_4[26]
PdZn(111)	HCOO	0.58	CH_3OH[27]
Ga_3Ni_5(221)	COOH	0.47	CH_3OH[28]
PdIn(110)/(211)	HCOO	0.05/-0.08	CH_3OH[29]

we report bimetallic alloys investigated so far for CO_2 conversion to C1 and C2 products.

To summarize Tab.1, the synergy of mixing two metals helps not only to activate CO_2 but also to stabilize the intermediates. The charge redistribution upon alloying metals alters the electronic structure, which helps achieve the desired activity. In general, it is observed that a specific composition of the bimetallic alloy exhibits higher reactivity compared to others. For example, PdCu is reported to be more reactive than $PdCu_3$ as the barrier for hydrogenation of CO_2 is less for PdCu (refer Tab.1). HCOO/COOH are two major intermediates for methanol formation and have a significant role in determining selectivity. Bagchi *et al.* reported that the absorption intensity and normalized absorbance of HCOO/COOH are relatively less in the case of Cu_9Ga_4 than $CuGa_2$, indicating a lower yield of methanol on Cu_9Ga_4.[30]

The literature shows that Cu is mainly alloyed with transition metals to produce C1/C2 hydrocarbons.[25,26,31–33] In contrast, no report on alloying Cu with non-transition metal, like Mg, for CO_2 conversion has been reported. A recent study observed that Mg nanoparticles could convert captured CO_2 to methane, methanol, and formic acid under ambient conditions.[34] Further, our group has investigated single-atom catalysts (SACs) of Cu(211), and Mg/Cu(211) is found to exhibit enhanced activity compared to transition metal SACs.[35] In the present work, we considered alloys of MgCu, which have not been studied so far to the best of our knowledge. We employed DFT to study the activation and hydrogenation of CO_2 on Mg_2Cu(224) and $MgCu_2$(311) facets. CO_2 chemisorbs on both the bimetallic alloys. For the hydrogenation of CO_2, the coadsorption of CO_2 with H_2O is examined. We observe that coadsorption leads to spontaneous hydrogenation of CO_2 to COOH over Mg_2Cu(224), whereas it has a negligible barrier over $MgCu_2$(311). Further, we investigate projected density of states (*pDOS*) and Mulliken charge to understand the observed catalytic activity.

Computational Details

All the calculations are carried out within the Kohn-Sham formalism of DFT. Projector Augmented Wave potential[36,37] is used, with Perdew Burke Ernzerhof (PBE) approximation for the exchange-correlation and generalized gradient approximation,[38,39] as implemented in planewave, pseudopotentials based code, Vienna Ab initio Simulation Package (*VASP*).[40–42] Van der Waals interactions are applied to account for the dispersion effect as implemented in the Grimme approach (DFT-D2).[43] Cifs for bulk Mg_2Cu and $MgCu_2$ are taken from the materials project.[44] The lattice constants are calculated and verified with the experimentally measured ones. For bulk Mg_2Cu, the calculated lattice parameters are a= 9.117 Å, b= 18.147 Å, and c= 5.220 Å which agree well with experimental values i.e. a= 9.102 Å, b= 18.198 Å, and c= 5.278 Å.[45] The calculated and experimental values of lattice constants for bulk $MgCu_2$ are a= b= c= 7.002 Å and 7.051 Å, respectively.[45] To model the surface, we considered the most dominant facets in the XRD;[45] accordingly, Mg_2Cu(224) and $MgCu_2$(311) are modeled. A slab of 2x1 with four layers is cleaved in (224) direction for Mg_2Cu and along (311) direction for $MgCu_2$ using VNL[46] with the bottom two layers fixed to mimic the bulk. K-point convergence is carried out by varying the k-mesh (MxNx1). Monkhorst-Pack grid of 5x3x1 for Mg_2Cu and 4x3x1 for $MgCu_2$ yields less than 0.001 eV variation in energy/atom and is used to sample the surface. This choice of Monkhorst-Pack grid resulted in 6 k-points in the IBZ for both alloys. A vacuum of 24.0 Å is sufficient to avoid interaction between adjacent images along the z-direction. Geometry optimization is carried out with a force cutoff of 0.01 eV/Å on the unfixed ions, and the total energies are converged below 10^{-4} eV for each SCF cycle. The activation barrier (E_a) is determined using the Climbing Image-Nudged Elastic Band (CI-NEB) method with three images and a force cutoff of 0.1 eV/Å.[47] The site-specific *pDOS* is calculated with denser k-mesh using LOBSTER.[48–51] Mulliken charges are computed to quantify the charge transfer between the surface and the adsorbate. E_{ads} is calculated using the formula: $E_{ads} = E_{system} - [E_{surface} + E_{adsorbate}]$ where E_{system} is the energy of the surface plus the adsorbate, $E_{surface}$ is the energy of the bare surface, and

$E_{adsorbate}$ is the energy of the adsorbate.

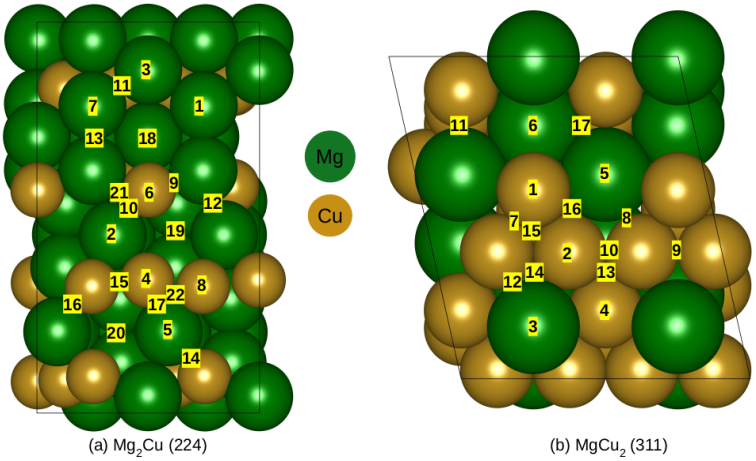

Figure 1: Schematic representation of bare facets; (a) $Mg_2Cu(224)$ and (b) $MgCu_2(311)$. Numbers represent unique sites for adsorption.

Results and discussion

Mg-Cu bimetallic alloys exist in two primary compositions, namely Mg_2Cu and $MgCu_2$. Mg_2Cu has an orthorhombic crystal structure, while $MgCu_2$ is cubic.[45] (224) and (311) are prominent peaks in XRD for Mg_2Cu and $MgCu_2$, respectively. Therefore, we modeled the $Mg_2Cu(224)$ and $MgCu_2(311)$ surfaces to explore their catalytic reactivity. A schematic

Table 2: We report the shortest M-C, Mg-O1, and Mg-O2 bond distances (M=Mg/Cu), C-O1/O2 bond elongation, ∠OCO, adsorption energy (E_{ads}), E_{eff} is effective adsorption energy obtained after removing the surface reconstruction contribution, calculated as E_{ads} - (E_{rec} - E_{clean}). E_{rec} is the energy of reconstructed surface and E_{clean} is the energy of bare surface. C and P are abbreviations used for chemisorbed and physisorbed geometry.

Class	M-C (Å)	Mg-O1 (Å)	Mg-O2 (Å)	C-O1 (Å)	C-O2 (Å)	∠OCO (^{0})	E_{ads} (eV)	E_{eff} (eV)	No. of cases
C-1	2.29-Mg	2.07	1.98	1.34	1.28	116.5	-3.61	-2.30	1
C-2	2.24-Mg	2.09	2.11	1.32	1.32	116.4	-3.32	-2.05	1
C-3	2.03-Cu	2.03	2.06	1.34	1.31	113.2	-3.32	-2.57	2
	1.97-Cu	2.09	2.06	1.34	1.29	116.9	-3.20	-2.32	
C-4	2.03-Cu	1.96	1.97	1.29	1.29	120.0	-3.02	-2.16	3
	2.01-Cu	1.95	1.97	1.29	1.29	120.0	-2.78	-2.15	
C-5	2.13-Cu	1.98	–	1.23	1.31	129.4	-0.74	–	2
P	>3.0	2.56	–	1.18	1.17	178.0	-0.39	–	13
		to 2.89				to 179.9	to -0.32	–	

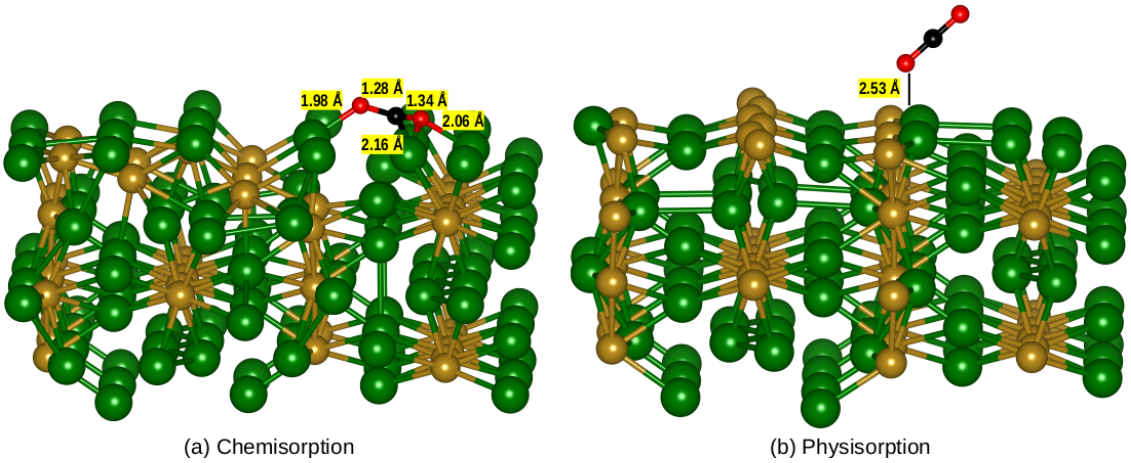

Figure 2: Adsorption geometries for CO_2 on $Mg_2Cu(224)$. (a) Chemisorbed: energetically most favorable and (b) physisorbed. Color code: Mg= Green, Cu= brown, C= black, and O= red.

view of $Mg_2Cu(224)$ and $MgCu_2(311)$, along with unique sites, is shown in Fig. 1-(a and b). For $Mg_2Cu(224)$, 22 optimizations are performed, whereas there are 17 unique positions scanned on the $MgCu_2(311)$ facet. The optimized configurations are broadly classified into two classes: physisorbed and chemisorbed. In the case of $MgCu_2(311)$, the chemisorbed structures could be further classified as weak and strong, depending upon adsorption energies and observed bond-angle. On both facets, chemisorption is energetically favored, and the bending of $\angle$OCO characterizes it. Details of various adsorption geometries for $Mg_2Cu(224)$ are tabulated in Tab. 2. C and P are abbreviations used for chemisorbed and physisorbed geometry. Representative chemisorbed and physisorbed CO_2 geometries are reported in Fig. 2. Strong chemisorption (as reflected in adsorption energies and bond-length activation) of CO_2 is observed near Mg because of the strong Mg-O interaction. Depending on how CO_2 adsorbs on the surface, there could be further sub-classification within chemisorption. For C-1 to C-4, we observe that CO_2 is adsorbed parallel to the surface plane; as a result, the surface is distorted. Further, the observed variation in E_{ads} for the same degree of activation in subclass C-4 is due to the difference in surface reconstruction (refer to Fig. SI-1). In C-5, CO_2 is adsorbed perpendicular to the surface plane with no surface reconstruction. On the other hand, in physisorption, the C-O bond-length is equivalent to that in molecular CO_2 (i.e., 1.18 Å) with a slight change in bond angle.

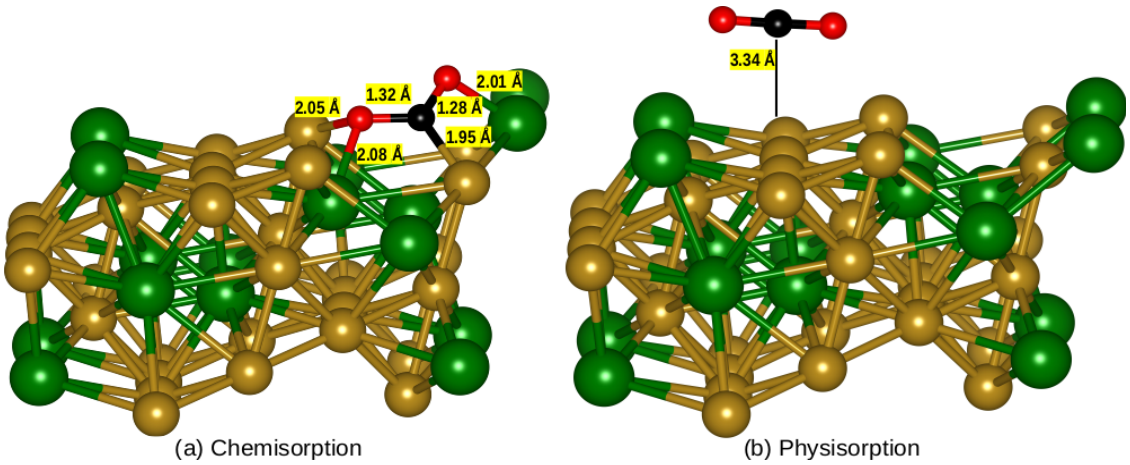

Figure 3: Adsorption geometries of CO_2 on $MgCu_2$(311). (a): Energetically most favorable adsorption and (b): physisorption. Color code: Mg= Green, Cu= brown, C= black, and O= red.

Table 3: We report the shortest M-C, M-O1, and M-O2 bond distances (M=Mg/Cu), C-O1/O2 bond elongation, ∠OCO, adsorption energy (E_{ads}), and no. of cases for a specific subclass. C, WC, and P are abbreviations for chemisorbed, weakly chemisorbed, and physisorbed geometries.

Class	M-C (Å)	Mg-O1 (Å)	Mg-O2 (Å)	C-O1 (Å)	C-O2 (Å)	∠OCO (^{0})	E_{ads} (eV)	No. of cases
C-1	1.96-Cu	2.01	2.09	1.32	1.28	118.9	-1.70	1
C-2	2.08-Cu	2.05	2.03	1.30	1.35	114.5	-1.56	2
C-3	2.15-Cu	2.01	2.05-Cu	1.28	1.28	124.7	-0.91	2
WC	∼3.0	∼2.4	–	1.17	1.19	178.7 to 176.4	∼ -0.48	8
P	>3.0	>3.0	–	1.18	1.18	178.5 to 179.2	-0.38 to -0.31	4

A representative case of chemisorption and physisorption for $MgCu_2$(311) is shown in Fig. 3, and the details like Metal-C/O bonds, adsorption energies, C-O bond lengths, and OCO bond angle for all optimized configurations are reported in Tab. 3. Although the overall trends of interaction between CO_2 and both these facets are similar, there are a few subtle differences. Unlike Mg_2Cu(224), surface reconstruction is not observed for $MgCu_2$(311) upon chemisorption. Chemisorption is accompanied by carbon binding to the surface Cu and not Mg in $MgCu_2$(311), as opposed to carbon and oxygen atoms connecting to surface Mg atoms for Mg_2Cu(224). Weak chemisorption (WC) is differentiated from physisorption based on the distance between CO_2 and the surface. The shortest distance between the surface and CO_2 is ∼2.4 Å in the case of WC, and the ∠OCO is bent by $\geq 2^0$ (refer to Tab. 3). Whereas,

when physisorbed, CO_2 is at a distance >3.0 Å from the surface.

Table 4: Mulliken charges (e^-) on C, O1, and O2 atoms of molecular CO_2 are compared with the ones after adsorption over Mg_2Cu(224) and $MgCu_2$(311). A negative value denotes a gain in charge.

Class	C	O1	O2	Class	C	O1	O2
CO_2	0.95	-0.47	-0.48	CO_2	0.95	-0.47	-0.48
		Mg_2Cu(224)				$MgCu_2$(311)	
C-1	0.25	-0.66	-0.64	C-1	0.28	-0.61	-0.58
C-2	0.21	-0.64	-0.63	C-2	0.26	-0.58	-0.66
C-3	0.26	-0.68	-0.64	C-3	0.30	-0.51	-0.51
C-4	0.30	-0.62	-0.61	–	–	–	–
C-5	0.29	-0.58	-0.45	WC	0.91	-0.40	-0.48
P	0.91	-0.43	-0.47	P	0.91	-0.45	-0.47

In Tab. 4, Mulliken charges on C, O1, and O2 when adsorbed on the Mg_2Cu(224) and $MgCu_2$(311) are reported. Variation in the effective charge on various atoms clearly distinguishes between chemisorbed and physisorbed CO_2. Also, the decreased positive charge on C indicates a gain in charge by carbon and oxygens. In the case of physisorption, the redistribution of charge is due to Van der Waals interaction with the surface. Overall we observe that CO_2 is strongly chemisorbed at Mg-rich sites on both surfaces because of the higher affinity of Mg toward oxygen than Cu.

Conversion of CO_2 to any of the value added products will have one of the following initial step. CO_2 will either dissociate to CO and O or partially hydrogenate to $COOH^*$ or $HCOO^*$. We have investigated all the three possibilities on both alloys. First, we study the dissociation of CO_2 to CO and O on both bimetallic alloys. Dissociation of CO_2 over Mg_2Cu(224) is an exothermic reaction with a barrier of 0.37 eV (refer to Fig. SI-2). On the other hand, at $MgCu_2$(311) energy barrier to cleave the C-O bond is 0.75 eV, twice that at Mg_2Cu(224) (refer Fig. SI-3). Moreover, the dissociation of CO_2 on the $MgCu_2$(311) is highly endothermic.

For the hydrogenation of CO_2 to $COOH^*/HCOO^*$, CO_2 and H_2O are coadsorbed, where H_2O serves as a source of hydrogen. We considered a 3x1 and a 3x2, 3-layered supercell for Mg_2Cu(224) and for $MgCu_2$(311), respectively. Thus, our supercell has 108 atoms, and the

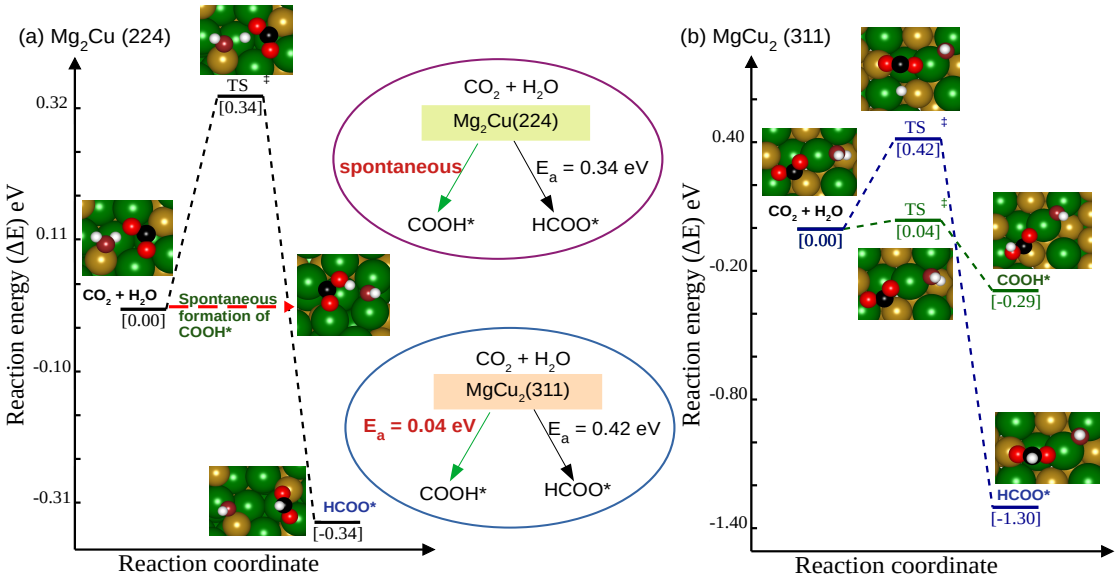

Figure 4: (a) $Mg_2Cu(224)$: COOH* forms spontaneously where as HCOO* has a barrier 0.34 eV. (b) $MgCu_2(311)$: The barrier for COOH* is negligible, whereas a barrier of 0.42 eV is to be crossed to from HCOO*. Color code: Mg= Green, Cu= brown, C= black, O(of CO_2)= red, H= white and O(of H_2O)= dark red.

bottom layer is fixed to mimic the bulk. Fig. 4 is a schematic representation of the reaction profile of CO_2 hydrogenation to COOH*/HCOO*. Interestingly, coadsorption leads to spontaneous formation of COOH* over $Mg_2Cu(224)$ as shown in Fig. 4-(a). On $MgCu_2(311)$, COOH* formation has a negligible barrier (0.04 eV). On the other hand, formation of HCOO* is kinetically unfavorable over both facets with comparatively higher barriers, i.e., 0.34 eV and 0.42 eV over $Mg_2Cu(224)$ and $MgCu_2(311)$, respectively.

The composition of the bimetallic alloys indeed plays a vital role in its activity. As we have seen $Mg_2Cu(224)$ is more reactive than to $MgCu_2(311)$ owing to the spontaneous hydrogenation to COOH*. In what follows, we bring out the correlation between the underlying electronic structure of these facets and their observed reactivity. In Fig. 5, we compare total Density of States (*tDOS*) of $Mg_2Cu(224)$ and $MgCu_2(311)$. We observe that more states are available near E_f for $Mg_2Cu(224)$ which correlates well with its higher activity. To gain further insights into the reactivity of $Mg_2Cu(224)$ and $MgCu_2(311)$, we examine *pDOS* of the surface atoms. As expected, 3d states of Cu lie well below the Fermi and hence do not contribute to reactivity (shown in Fig. SI-4). The presence of inequivalent Mg and

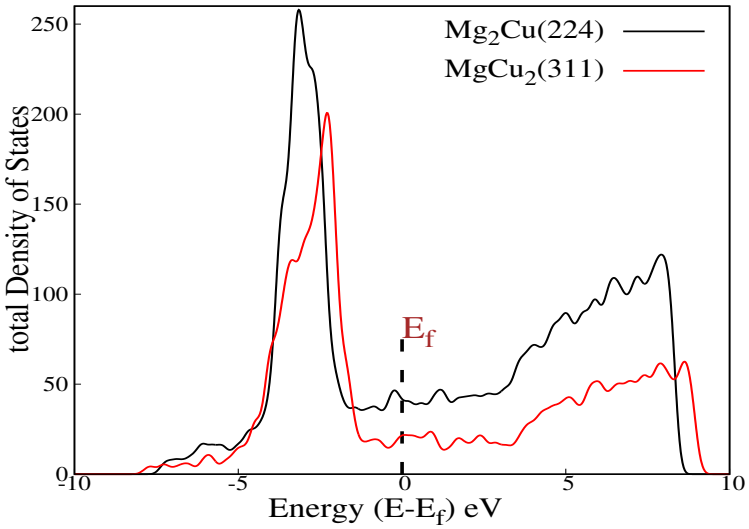

Figure 5: *tDOS* for bare $Mg_2Cu(224)$ and $MgCu_2(311)$ surfaces. Fermi energy (E_f) is set to coincide with 0 eV.

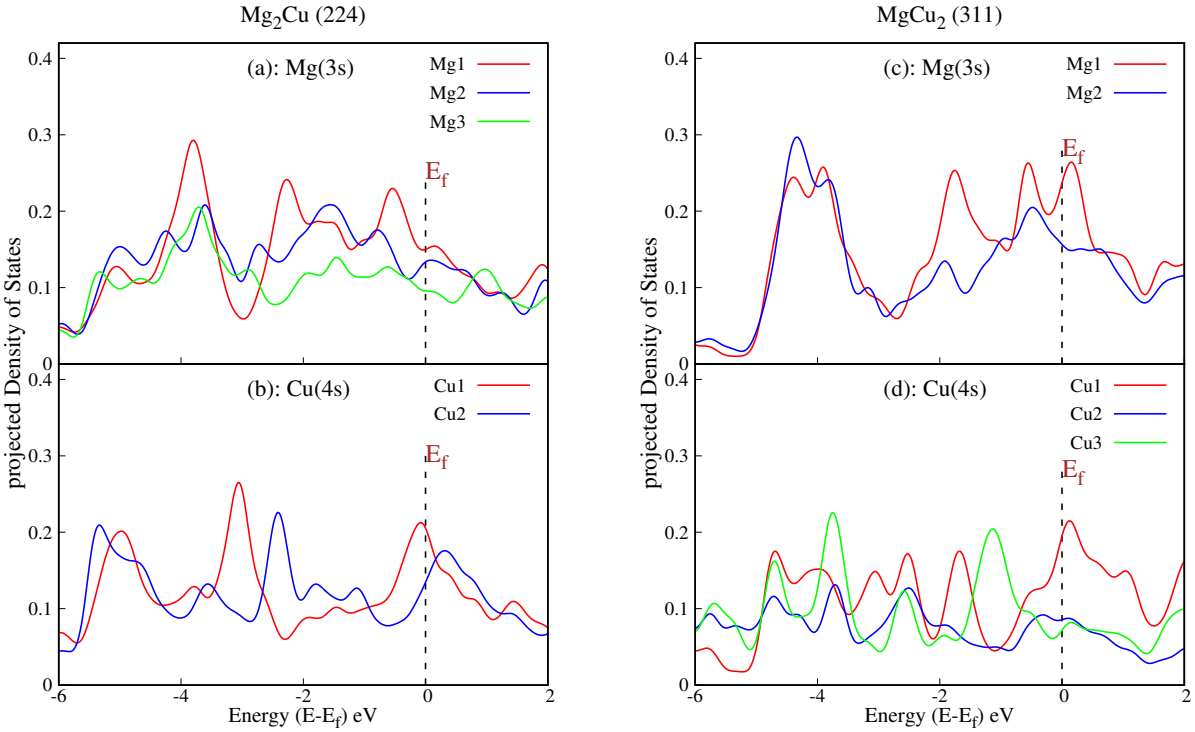

Figure 6: *pDOS* of (3s) states of Mg and (4s) states of Cu: (a) and (b) for bare $Mg_2Cu(224)$ and (c) and (d) for bare $MgCu_2$ (311). Fermi energy (E_f) is set to coincide with 0 eV.

Cu atoms on $Mg_2Cu(224)$ and $MgCu_2(311)$ facets is evident from the distinguishable *pDOS* shown in Fig. 6. The distinct Cu and Mg atoms are shown in Fig. SI-5 for clarity. In case of Mg_2Cu, there are three "types" of Mg and two "types" of Cu as shown in Fig. 6-(a and b).

For $MgCu_2$, there are two "types" of Mg and three "types" of Cu atoms as shown in Fig. 6-(c and d). We observe a higher peak intensity near E_f for the surface Mg1/Cu1 atoms. These under-coordinated surface atoms are more reactive than well-coordinated lower-step atoms. Interestingly, Mg1 at $MgCu_2(311)$ has higher peak intensity near E_f than at $Mg_2Cu(224)$. However, the number of such Mg atoms is less in $MgCu_2(311)$ than $Mg_2Cu(224)$, which makes latter more reactive. Further, 4s states for both Cu atoms in $Mg_2Cu(224)$ have collectively high peak intensity at E_f compared to the ones at $MgCu_2(311)$. In short, Mg and Cu sites are more reactive in $Mg_2Cu(224)$ over $MgCu_2(311)$. Additionally, more Mg atoms at the $Mg_2Cu(224)$ surface adds to its reactivity. The Mulliken charges on these Mg atoms is around 0.10 to 0.18 e^-. On the other hand, $MgCu_2(311)$ has Mg coordinated to more Cu atoms at the surface and subsurface. The Mulliken charges on them are noted to be around 0.50 e^-. Thus, $Mg_2Cu(224)$ has more electron density than $MgCu_2(311)$, as observed from *tDOS*, *pDOS*, and Mulliken charges on Mg. It can easily donate its charge, so coadsorption leads to the spontaneous formation of COOH.

CO_2 hydrogenation to $COOH^*/HCOO^*$ is a key factor in determining the reaction pathway for producing alcohols/hydrocarbons. As reported in Tab. 1, Cu-based alloys have a barrier greater than 0.4 eV for CO_2 hydrogenation to COOH/HCOO. Our investigations reveal that the Mg-Cu bimetallic alloys studied in the present work exhibit better catalytic activity towards CO_2 hydrogenation to $COOH^*/HCOO^*$ than already reported ones. Further, over PdIn alloys, the formation of HCOO is almost spontaneous,[29] while our study reports spontaneous hydrogenation to COOH over Mg-Cu alloys. Pd and In are precious metals; hence, alloying them may increase the production cost, and thus cheaper alternatives are desirable. We propose alloying two earth-abundant metals Cu and Mg, which gives activity greater or comparable to the already reported ones as discussed above. Additionally, using H_2O as a hydrogen source is a green and economical way to produce value-added products from CO_2 and awaits experimental verification.

Conclusion

Conversion of CO_2 to value-added chemicals is one of the sought for approach to reduce the carbon footprint. In the present work, we demonstrate that MgCu alloys have the least barrier for hydrogenation of CO_2 compared to the reported studies. Coadsorption of CO_2 with water leads to the spontaneous formation of COOH* on $Mg_2Cu(244)$, whereas it has a negligible barrier (0.04 eV) on $MgCu_2(311)$. Another hydrogenation path, i.e., formation of HCOO*, has a barrier of 0.34 eV and 0.42 eV on these facets. Dissociation of CO_2 to CO has a barrier of 0.37 eV and 0.75 eV on $Mg_2Cu(224)$ and $MgCu_2(311)$, respectively. Thus, hydrogenation of CO_2 is favored over dissociation on MgCu alloys. Our studies also reveal the underlying electronic structure as evident from *pDOS* and Mulliken charges which explains the observed trends. Finally, We conclude that Mg-Cu bimetallic alloys, i.e., $Mg_2Cu(224)$ and $MgCu_2(311)$, are potential candidates for CO_2 activation and conversion and need to be explored experimentally.

Acknowledgement

Authors gratefully acknowledges CSIR Fourth Paradigm Institute and National Supercomputing Mission (NSM) for providing computing resources of "PARAM Brahma" at IISER Pune, which is implemented by C-DAC and supported by the Ministry of Electronics and Information Technology (MeitY) and Department of Science and Technology (DST), Government of India. KT acknowledges CSIR for research fellowship.

Supporting Information Available

Supporting information is available and contains: Table for Mulliken charges for CO_2 adsorption on $MgCu_2(311)$, and energy profile for CO_2 dissociation over $Mg_2Cu(224)$ and $MgCu_2(311)$, *pDOS*:Cu-(3d) at $MgCu_2(311)$ and $Mg_2Cu(224)$.

References

(1) Hepburn, C.; Adlen, E.; Beddington, J.; Carter, E. A.; Fuss, S.; Mac Dowell, N.; Minx, J. C.; Smith, P.; Williams, C. K. The technological and economic prospects for CO2 utilization and removal. *Nature* **2019**, *575*, 87–97.

(2) Al-Ghussain, L. Global warming: Review on driving forces and mitigation. *Environmental Progress & Sustainable Energy* **2019**, *38*, 13–21.

(3) Zhang, S.; Wu, Z.; Liu, X.; Hua, K.; Shao, Z.; Wei, B.; Huang, C.; Wang, H.; Sun, Y. A short review of recent advances in direct CO2 hydrogenation to alcohols. *Topics in Catalysis* **2021**, *64*, 371–394.

(4) Braga, A. H.; Vidinha, P.; Rossi, L. M. Hydrogenation of carbon dioxide: from waste to value. *Current Opinion in Green and Sustainable Chemistry* **2020**, *26*, 100386.

(5) Podrojková, N.; Sans, V.; Oriňak, A.; Oriňaková, R. Recent developments in the modelling of heterogeneous catalysts for CO2 conversion to chemicals. *ChemCatChem* **2020**, *12*, 1802–1825.

(6) Liu, X.; Sun, L.; Deng, W.-Q. Theoretical investigation of CO2 adsorption and dissociation on low index surfaces of transition metals. *The Journal of Physical Chemistry C* **2018**, *122*, 8306–8314.

(7) Wong, Y.; Choi, Y. H.; Tanaka, S.; Yoshioka, H.; Mukai, K.; Halim, H. H.; Mohamed, A. R.; Inagaki, K.; Hamamoto, Y.; Hamada, I., et al. Adsorption of CO2 on Terrace, Step, and Defect Sites on Pt Surfaces: A Combined TPD, XPS, and DFT Study. *The Journal of Physical Chemistry C* **2021**, *125*, 23657–23668.

(8) Czelej, K.; Cwieka, K.; Kurzydlowski, K. J. CO2 stability on the Ni low-index surfaces: van der Waals corrected DFT analysis. *Catalysis Communications* **2016**, *80*, 33–38.

(9) Mendes, P. C.; Verga, L. G.; Da Silva, J. L. Ab initio screening of Pt-based transition-metal nanoalloys using descriptors derived from the adsorption and activation of CO 2. *Physical Chemistry Chemical Physics* **2021**, *23*, 6029–6041.

(10) Santiago-Rodríguez, Y.; Barreto-Rodríguez, E.; Curet-Arana, M. C. Quantum mechanical study of CO2 and CO hydrogenation on Cu (111) surfaces doped with Ga, Mg, and Ti. *Journal of Molecular Catalysis A: Chemical* **2016**, *423*, 319–332.

(11) Ko, J.; Kim, B.-K.; Han, J. W. Density functional theory study for catalytic activation and dissociation of CO2 on bimetallic alloy surfaces. *The Journal of Physical Chemistry C* **2016**, *120*, 3438–3447.

(12) Ye, Y.; Qian, J.; Yang, H.; Su, H.; Lee, K.-J.; Etxebarria, A.; Cheng, T.; Xiao, H.; Yano, J.; Goddard III, W. A., et al. Synergy between a silver–copper surface alloy composition and carbon dioxide adsorption and activation. *ACS applied materials & interfaces* **2020**, *12*, 25374–25382.

(13) Kumar, A.; Ropital, F.; de Bruin, T.; Diawara, B. Effects of surface orientations of Cr2O3 on CO2 adsorption: A DFT approach. *Applied Surface Science* **2020**, *529*, 147127.

(14) Li, X.; Paier, J. Vibrational properties of CO2 adsorbed on the Fe3O4 (111) surface: Insights gained from DFT. *The Journal of Chemical Physics* **2020**, *152*, 104702.

(15) Mino, L.; Spoto, G.; Ferrari, A. M. CO2 capture by TiO2 anatase surfaces: a combined DFT and FTIR study. *The Journal of Physical Chemistry C* **2014**, *118*, 25016–25026.

(16) Tang, Q.-L.; Luo, Q.-H. Adsorption of CO2 at ZnO: a surface structure effect from DFT+ U calculations. *The Journal of Physical Chemistry C* **2013**, *117*, 22954–22966.

(17) Ye, R.-P.; Ding, J.; Gong, W.; Argyle, M. D.; Zhong, Q.; Wang, Y.; Russell, C. K.;

Xu, Z.; Russell, A. G.; Li, Q., et al. CO2 hydrogenation to high-value products via heterogeneous catalysis. *Nature communications* **2019**, *10*, 1–15.

(18) Li, M. M.-J.; Tsang, S. C. E. Bimetallic catalysts for green methanol production via CO 2 and renewable hydrogen: a mini-review and prospects. *Catalysis Science & Technology* **2018**, *8*, 3450–3464.

(19) Kang, L.; Chen, X.; Ke, Q. Theoretical study on the synthesis of methane by CO2 hydrogenation on Ni3Fe (111) surface. *Journal of Natural Gas Science and Engineering* **2021**, *94*, 104114.

(20) Cui, M.; Johnson, G.; Zhang, Z.; Li, S.; Hwang, S.; Zhang, X.; Zhang, S. AgPd nanoparticles for electrocatalytic CO 2 reduction: bimetallic composition-dependent ligand and ensemble effects. *Nanoscale* **2020**, *12*, 14068–14075.

(21) Sun, Y.; Hu, H.; Wang, Y.; Gao, J.; Tang, Y.; Wan, P.; Hu, Q.; Lv, J.; Zhang, T.; Yang, X. J. In situ hydrogenation of CO2 by Al/Fe and Zn/Cu alloy catalysts under mild conditions. *Chemical Engineering & Technology* **2019**, *42*, 1223–1231.

(22) Studt, F.; Sharafutdinov, I.; Abild-Pedersen, F.; Elkjær, C. F.; Hummelshøj, J. S.; Dahl, S.; Chorkendorff, I.; Nørskov, J. K. Discovery of a Ni-Ga catalyst for carbon dioxide reduction to methanol. *Nature chemistry* **2014**, *6*, 320–324.

(23) Lin, S.; Wang, Q.; Li, M.; Hao, Z.; Pan, Y.; Han, X.; Chang, X.; Huang, S.; Li, Z.; Ma, X. Ni–Zn Dual Sites Switch the CO2 Hydrogenation Selectivity via Tuning of the d-Band Center. *ACS Catalysis* **2022**, *12*, 3346–3356.

(24) Li, M. M.-J.; Zou, H.; Zheng, J.; Wu, T.-S.; Chan, T.-S.; Soo, Y.-L.; Wu, X.-P.; Gong, X.-Q.; Chen, T.; Roy, K., et al. Methanol synthesis at a wide range of H2/CO2 ratios over a Rh-In bimetallic catalyst. *Angewandte Chemie* **2020**, *132*, 16173–16180.

(25) Nie, X.; Jiang, X.; Wang, H.; Luo, W.; Janik, M. J.; Chen, Y.; Guo, X.; Song, C. Mechanistic understanding of alloy effect and water promotion for Pd-Cu bimetallic catalysts in CO2 hydrogenation to methanol. *ACS Catalysis* **2018**, *8*, 4873–4892.

(26) Nie, X.; Wang, H.; Janik, M. J.; Chen, Y.; Guo, X.; Song, C. Mechanistic insight into C–C coupling over Fe–Cu bimetallic catalysts in CO2 hydrogenation. *The Journal of Physical Chemistry C* **2017**, *121*, 13164–13174.

(27) Brix, F.; Desbuis, V.; Piccolo, L.; Gaudry, É. Tuning adsorption energies and reaction pathways by alloying: PdZn versus Pd for CO2 hydrogenation to methanol. *The Journal of Physical Chemistry Letters* **2020**, *11*, 7672–7678.

(28) Tang, Q.; Shen, Z.; Huang, L.; He, T.; Adidharma, H.; Russell, A. G.; Fan, M. Synthesis of methanol from CO 2 hydrogenation promoted by dissociative adsorption of hydrogen on a Ga 3 Ni 5 (221) surface. *Physical Chemistry Chemical Physics* **2017**, *19*, 18539–18555.

(29) Wu, P.; Yang, B. Intermetallic PdIn catalyst for CO 2 hydrogenation to methanol: mechanistic studies with a combined DFT and microkinetic modeling method. *Catalysis Science & Technology* **2019**, *9*, 6102–6113.

(30) Bagchi, D.; Raj, J.; Singh, A. K.; Cherevotan, A.; Roy, S.; Manoj, K. S.; Vinod, C.; Peter, S. C. Structure-Tailored Surface Oxide on Cu–Ga Intermetallics Enhances CO2 Reduction Selectivity to Methanol at Ultralow Potential. *Advanced Materials* **2022**, *34*, 2109426.

(31) Jeon, Y. E.; Ko, Y. N.; Kim, J.; Choi, H.; Lee, W.; Kim, Y. E.; Lee, D.; Kim, H. Y.; Park, K. T. Selective production of ethylene from CO2 over CuAg tandem electrocatalysts. *Journal of Industrial and Engineering Chemistry* **2022**, *116*, 191–198.

(32) Huang, J.; Dai, J.; Zhu, J.; Chen, R.; Fu, X.; Liu, H.; Li, G. Bimetallic Au-Cu gradient

alloy for electrochemical CO2 reduction into C2H4 at low overpotential. *Journal of Catalysis* **2022**, *415*, 134–141.

(33) Din, I. U.; Alotaibi, M. A.; Alharthi, A. I.; Al-Shalwi, M. N.; Alshehri, F. Green synthesis approach for preparing zeolite based Co-Cu bimetallic catalysts for low temperature CO2 hydrogenation to methanol. *Fuel* **2022**, *330*, 125643.

(34) Rawool, S. A.; Belgamwar, R.; Jana, R.; Maity, A.; Bhumla, A.; Yigit, N.; Datta, A.; Rupprechter, G.; Polshettiwar, V. Direct CO 2 capture and conversion to fuels on magnesium nanoparticles under ambient conditions simply using water. *Chemical science* **2021**, *12*, 5774–5786.

(35) Thakkar, K.; Joshi, K. Single-atom alloys of Cu(211) with earth-abundant metals for enhanced activity toward CO2 dissociation. *to be communicated* **2022**,

(36) Blöchl, P. E. Projector augmented-wave method. *Physical Review B* **1994**, *50*, 17953–17979.

(37) Kresse, G.; Joubert, D. From ultrasoft pseudopotentials to the projector augmented-wave method. *Physical Review B* **1999**, *59*, 1758–1775.

(38) Perdew, J. P.; Burke, K.; Ernzerhof, M. Generalized Gradient Approximation Made Simple. *Physical Review Letters* **1996**, *77*, 3865–3868.

(39) Perdew, J. P.; Burke, K.; Ernzerhof, M. Generalized Gradient Approximation Made Simple [Phys. Rev. Lett. 77, 3865 (1996)]. *Physical Review Letters* **1997**, *78*, 1396–1396.

(40) Kresse, G.; Hafner, J. *Ab initio* molecular-dynamics simulation of the liquid-metal–amorphous-semiconductor transition in germanium. *Physical Review B* **1994**, *49*, 14251–14269.

(41) Kresse, G.; Furthmüller, J. Efficient iterative schemes for *ab initio* total-energy calculations using a plane-wave basis set. *Physical Review B* **1996**, *54*, 11169–11186.

(42) Kresse, G.; Furthmüller, J. Efficiency of ab-initio total energy calculations for metals and semiconductors using a plane-wave basis set. *Computational Material Science* **1996**, *6*, 15–50.

(43) Grimme, S. Semiempirical GGA-type density functional constructed with a long-range dispersion correction. *Journal of computational chemistry* **2006**, *27*, 1787–1799.

(44) Jain, A.; Ong, S. P.; Hautier, G.; Chen, W.; Richards, W. D.; Dacek, S.; Cholia, S.; Gunter, D.; Skinner, D.; Ceder, G.; Persson, K. a. The Materials Project: A materials genome approach to accelerating materials innovation. *APL Materials* **2013**, *1*, 011002.

(45) Shao, H.; Wang, Y.; Xu, H.; Li, X. Preparation and hydrogen storage properties of nanostructured Mg2Cu alloy. *Journal of Solid State Chemistry* **2005**, *178*, 2211–2217.

(46) Stradi, D.; Jelver, L.; Smidstrup, S.; Stokbro, K. Method for determining optimal supercell representation of interfaces. *Journal of Physics: Condensed Matter* **2017**, *29*, 185901.

(47) Henkelman, G.; Uberuaga, B. P.; Jónsson, H. A climbing image nudged elastic band method for finding saddle points and minimum energy paths. *The Journal of chemical physics* **2000**, *113*, 9901–9904.

(48) Dronskowski, R.; Blöchl, P. E. Crystal orbital Hamilton populations (COHP): energy-resolved visualization of chemical bonding in solids based on density-functional calculations. *The Journal of Physical Chemistry* **1993**, *97*, 8617–8624.

(49) Deringer, V. L.; Tchougréeff, A. L.; Dronskowski, R. Crystal orbital Hamilton population (COHP) analysis as projected from plane-wave basis sets. *The Journal of Physical Chemistry A* **2011**, *115*, 5461–5466.

(50) Maintz, S.; Deringer, V. L.; Tchougréeff, A. L.; Dronskowski, R. Analytic projection from plane-wave and PAW wavefunctions and application to chemical-bonding analysis in solids. *Journal of Computational Chemistry* **2013**, *34*, 2557–2567.

(51) Maintz, S.; Deringer, V. L.; Tchougréeff, A. L.; Dronskowski, R. LOBSTER: A tool to extract chemical bonding from plane-wave based DFT. *Journal of Computational Chemistry* **2016**, *37*, 1030–1035.